frontiers in Materials

ORIGINAL RESEARCH
published: 20 March 2020
doi: 10.3389/fmats.2020.00055

Microstructural Characteristics, Mechanical and Corrosion Properties of an Extruded Low-Alloyed Mg-Bi-Al-Zn Alloy

Wei-li Cheng[1,2]*, *Yan-hui Liu*[2], *Shi-chao Ma*[3], *Li-fei Wang*[1,2], *Hong-xia Wang*[1,2] and *Xiao-feng Niu*[1,2]

[1] Shanxi Key Laboratory of Advanced Magnesium-Based Materials, Taiyuan University of Technology, Taiyuan, China, [2] School of Materials Science and Engineering, Taiyuan University of Technology, Taiyuan, China, [3] School of Materials Science and Engineering, Dalian University of Technology, Dalian, China

An extruded low-alloyed Mg-Bi-Al-Zn alloy combining excellent tensile properties (YS = 201 MPa, EL = 29. 4%) with high corrosion resistance (P_i = 0.14 mm/a) for biomedical application is successfully developed in this study. The extruded alloy is mainly composed of dynamic recrystallized (DRXed) grains (2.32 ± 0.12 μm) and strongly textured coarse non-DRXed grains, as well as certain nano-scaled Mg_3Bi_2 precipitates (135.68 ± 27.86 nm). Note that most basal planes for non-DRXed grains are preferentially distributed parallel to the extrusion direction. The study explored the dependences of the properties and relevant mechanisms of the studied alloy on its microstructural characteristics in terms of grain size, grain orientation, and precipitates.

Keywords: Mg-Bi-Al-Zn alloy, microstructure, tensile properties, texture, corrosion behavior

OPEN ACCESS

Edited by:
Antonio Caggiano, Darmstadt University of Technology, Germany

Reviewed by:
Qiang Yang, Chinese Academy of Sciences, China
Sung Bo Lee, Seoul National University, South Korea

***Correspondence:**
Wei-li Cheng
chengweili7@126.com

Specialty section:
This article was submitted to Structural Materials, a section of the journal Frontiers in Materials

Received: *29 November 2019*
Accepted: *21 February 2020*
Published: *20 March 2020*

Citation:
Cheng W, Liu Y, Ma S, Wang L, Wang H and Niu X (2020) Microstructural Characteristics, Mechanical and Corrosion Properties of an Extruded Low-Alloyed Mg-Bi-Al-Zn Alloy. Front. Mater. 7:55. doi: 10.3389/fmats.2020.00055

INTRODUCTION

Due to the biodegradation nature of human bio-environment without the need for second surgeries to remove implants and favorable biological properties of magnesium ions released, Mg-based alloys, as potentially biodegradable implant materials, receive increasing attention (Esmaily et al., 2017). The rapid degradation of such alloys probably restricts application of the alloys as implant materials. Moreover, during the degradation process, Mg-based alloy implants potentially present gradually deteriorating mechanical properties (Bakhsheshi-Rad et al., 2016).

Alloying proves to be the most fundamental way of improving mechanical properties and corrosion resistance of magnesium alloys, due to the efficiency and low cost of the process. It is reported that adding the cost-effective element bismuth (Bi) to Mg-based alloys could improve the mechanical properties and resistance to corrosion simultaneously when Bi presents in the α-Mg matrix with solutionized state and/or nano-scaled Mg-Bi precipitates (Tok et al., 2015; Majhi and Mondal, 2019). Bi has positive effects as it is able to form a thermally stable Mg_3Bi_2 phase in the Mg alloys and because of its non-toxicity (He et al., 2019; Meng et al., 2020). Further, it is essential to introduce Al as a type of alloying element in applications that require grain refinement, thicker film formation, and castability (Lv et al., 2020). Meanwhile, it has been reported repeatedly that the protective feature displayed by pseudo-passive layers that are formed naturally on metal surfaces could be improved by Al addition (Goli and Aghajani, 2018). Moreover, it is commonly accepted that adding Zn in Mg alloys is demonstrated to contribute to the improvement of mechanical properties and corrosion through the reduction of impurities (Jina et al., 2019). A previous report

indicates that Zn is among the richest essential elements in the human body and Zn ions released are absorbable (Wang et al., 2017). Furthermore, it is well known that high alloying generally leads to a great amount of second-phase particles, which promotes the formation of microgalvanic couples and thus accelerates corrosion processing. Taking both the mechanical properties and the corrosion behavior into consideration, micro alloying seems to be the best way to balance them and to possibly decrease the harmful effects related to alloying elements. Based on the abovementioned points, a low-alloyed Mg-1Bi-1Al-1Zn alloy system is chosen for investigation of its potential as a material to produce biodegradable implants.

In general terms, the corrosion performance of alloys based on Mg is influenced by grain size, second-phase particle, dissolved alloying element, and grain orientation. The deformation process, such as extrusion, is a feasible option to tailor the microstructure of grain size, orientation, and second phase for improved mechanical properties and corrosion resistance of Mg alloys. The grain size has obvious effect on the corrosion rate relative to Mg alloys in terms of diffusion rate and coordination reactivity. A previous work indicated that one order of magnitude decrease in corrosion rate could be achieved between ultrafine and coarsest grained microstructure of the wrought Mg alloys (Argade et al., 2012). Moreover, the ultrafine grain showed highest polarization resistance compared to the coarsest one (Luo et al., 2020). Recently, many reports indicate that second phases that function as cathodic phases could accelerate Mg substrate to be corroded and dissolved (Feng et al., 2017), and Zeng et al. pointed out that decreasing volume fraction of particles of the second phase led to improving resistance of Mg alloys to corrosion (Zeng et al., 2015). In addition, Liu et al. reported that the impedance of AZ91 alloys with the presence of finer nanometer particles of $Mg_{17}Al_{12}$ phase in 0.6 M NaCl solution increased from 300 to 500 Ω due to the decreased susceptibility of microgalvanic corrosion (Liu et al., 2018). In addition, a previous report (Hagihara et al., 2016) indicates the dependence of corrosion properties of Mg and its alloys upon crystal orientation, with resistance to corrosion increasing according to the order (102) < (113) < (100) < (110) < (0001). This is related to the surface energy. The closely packed crystallographic plane has a higher atomic coordination, a higher binding energy, and thus a lower surface energy and a higher activation energy for dissolution compared with the loosely packed crystallographic plane. As a result, tailoring the alloy microstructure underpins the improvement of comprehensive properties for Mg alloys.

So far, extrusion is an effective strengthening method to enhance properties of Mg alloys through microstructure controlling. Recently, many studies focused on the effect of various alloying elements on the corrosion performance of extruded Mg alloys. However, the combined effects of grain boundary with crystallographic texture upon corrosion resistance of low-alloyed Mg alloy containing rarely few nano-scaled particles remain to be clarified. Considering this, the current study developed an as-extruded low-alloyed Mg-Bi-Al-Zn alloy system with textured bimodal structure, which possesses a great balance between mechanical properties and corrosion resistance. Further, the dependence of corrosion resistance and tensile properties upon microstructural features (grain boundary, nano-scale precipitates, grain orientation) was also discussed in extruded condition.

TABLE 1 | Chemical composition of the extruded Mg-Bi-Al-Zn alloy determined by ICP-OES.

Specimen	Chemical composition (wt.%)						
	Mg	Bi	Al	Zn	Fe	Cu	Si
Extruded	Bal.	0.9726	0.9617	0.9803	0.0021	0.0002	0.0030

MATERIALS AND METHODS

Sample Preparation

The Mg-1.0 Bi-1.0 Al-1.0 (wt.%) Zn alloy was fabricated in a vacuum melting furnace through melting Mg, Bi, Al, and Zn with 99.9% purity in an atmosphere of CO_2 and SF_6 for preventing oxidation. Researchers then conducted solid solution treatment (SST) for 1 h at 320°C and 3 h at 500°C with cold water quenching at room temperature to obtain a more homogeneous microstructure. Direct extrusion experiments were implemented at an initial billet temperature of 300°C, a ram speed of 0.1 mm s^{-1}, and an extrusion ratio of 16. Extruded rods with a section diameter of 10 mm were obtained.

Microstructure Analysis

A TESCAN MIRA3 scanning electron microscope (SEM) equipped with energy dispersive X-ray (EDS) and electron back-scatter diffraction (EBSD) was used to observe the microstructural characteristics and texture of the samples. The chemical composition of the extruded alloy determined by optical emission spectroscopy (ICP-OES) is listed in **Table 1**. Furthermore, samples were subjected to Cu-Kα, Y-2000 X-ray diffraction (XRD) to determine alloy phases and a Rigaku D/max-2500PC XRD to obtain the pole figure. XRD patterns were analyzed with the software MDI Jade 6.0. Chemical components of corrosion products of extruded alloy were tested adopting a K-Alphav X-ray photo-electron spectroscope (XPS). Measurements were performed using an adventitious C1s signal, set to be 284.6 eV for values of all binding energy in XPS spectra.

Tensile Tests

Tensile specimens measuring 18 mm gauge × 4 mm gauge × 2 mm gauge (length × width × thickness) were sliced along the extrusion direction (ED) from the extruded rod. Afterwards, researchers conducted tensile tests applying a DNS100 electric testing machine at the initial strain rate of 1×10^{-3} s^{-1} and room temperature.

Corrosion Tests

Hydrogen evolution test was measured by ASTM G31-72 using 1 cm^2 ground specimens at 37°C in simulated body fluid (SBF). Specimens were placed in a tube that is tightly sealed, with solution volume showing a ratio of 25:1 ml/cm^2 to the area of specimens. The equation for corrosion rate (C_R) of extruded

alloys based on hydrogen evolution rate (V_H) is (Shi and Atrens, 2011):

$$C_R(\text{mm}/y) = 2.279 V_H(ml/cm^2/d) \quad (1)$$

Electrochemical properties of the studied alloy in SBF solution was studied by performing potentiodynamic polarization (PDP) test and electrochemical impedance spectroscopy (EIS) measurements on an electrochemical workstation equipped with a CorrTest Land CS350 (Wuhan, China) electrochemical system. A three-electrode cell, platinum mesh, and the specimen, separately taken as reference electrode, counter electrode, and working electrode (exposing an area of 1 cm^2 in SBF solution), were connected to the potentiostat. After holding the specimens in open circuit potential (OCP) for 50 min, PDP tests were conducted while scanning in the range of ±300 mV/SCE at 0.5 mV/SCE s^{-1}. The formula of corrosion rate (P_i) is (Shi et al., 2010):

$$P_\text{i} = 22.85 i_{corr} \quad (2)$$

The following formula was used to calculate polarization resistance (R_p) based on electrochemical parameters (i_corr, β_a, and β_a) (Shi et al., 2010):

$$R_p = \frac{\beta_a \beta_c}{2.3(\beta_a + \beta_c) i_{corr}} \quad (3)$$

The EIS measurement was conducted with an amplitude signal of 10 mV at OCP at a frequency of 100 kHz−10 mHz. Zview-Impedance Software was used to fit the related results, showing fitting errors for parameters within 5%. All tests were repeated three times to guarantee the reliability of the results.

RESULTS AND DISCUSSION

Microstructure Analysis

The EBSD observation results of the extruded Mg-Bi-Al-Zn alloy are illustrated in **Figure 1**, which indicates that the extruded alloy presents bimodal microstructure consisting of dynamically recrystallized (DRXed) fine grains showing AGS being 2.32 ± 0.12 μm and highly textured unDRXed coarse grains (**Figures 1a,d**). The volume fraction of dynamic recrystallization (f_DRX) is 87.72% in **Figure 1d**. The inverse pole figures displayed in **Figures 1a–c** underscore crystal orientations for complete Mg grains and only elongated grains, indicative of elongated grains being highly textured. The α-Mg grains represent basal (B) crystal orientation where regions in red are expressed as G(B) with non-basal (NB) crystal planes with regions in other colors indicated by G(NB) such as those in the present study. In the grain boundary map (**Figure 1b**), low-angle grain boundaries (LAGBs) having misorientation lower than 15° are characterized by red lines. It can be seen that the fraction of the LAGBs is significantly larger in Mg grains having basal plane parallel to surfaces compared to that of the non-basal plane. An inverse pole figure in three regions of the remaining original grains is shown in **Figure 1c**, with the corresponding (0001) pole figure containing only elongated grains inserted in it. Further, the Schmid factor exceeds 0.2 in most grains of extruded alloys with average Schmid factor being 0.357 (**Figure 1e**), and the fraction of LAGBs is rather higher compared to other ranges of equivalence (**Figure 1f**).

Figure 2 depicts the XRD patterns and SEM high-magnification image with EDS results of the studied alloy. XRD patterns therein reveal two groups of peaks, for Mg_3Bi_2 and α-Mg phases separately. Accordingly, a few nano-scaled Mg_3Bi_2 precipitate particles with an average size of 135.68 ± 27.86 nm are distributed along the boundary and in the interior of grains (**Figure 2b**). The formation of the nano-scaled precipitates, commonly seen in extruded Mg alloys, is attributed to the appearance of dynamic precipitation in the extrusion process (Cheng et al., 2017).

Mechanical Behaviors

Figure 3A shows the tensile stress–strain curve and fracture surface of the studied alloy. Results show that extruded alloys have ultimate tensile strength (UTS), elongation (EL), and yield strength (YS) of 247 MPa, 29.4%, and 201 MPa, respectively. The perfect integration of ductility and strength can be usually explained from perspectives of bimodal structure, texture, and dislocations as well as the distribution of precipitates. Firstly, strength and ductility can be effectively improved by the bimodal structure due to the strong texture strengthening of the unDRXed grains and grain boundary strengthening of the fine DRXed grains (Yamasaki et al., 2011; Wang et al., 2015). In line with the Hall–Petch equation, finer grains exhibit excellent yield strength. Secondly, the basal texture shows a maximum intensity of 3.7 based on the (0002) pole figure of extruded alloys (**Figure 3B**). Grains are found to have c-axis preferentially lying on ND-ED plane and [0002] directions parallel to ED, representative features of as-extruded Mg alloys (Laser et al., 2008). Further, when the stress is applied parallel to the basal plane, it is difficult to activate the basal slip, leading to high strength. Texture distribution in extruded alloys with most of the grains parallel to the ED renders activation of basal slip difficult, thus enhancing yield strength. Thirdly, it can be seen from **Figure 1b** that LAGBs characterized by red lines in the deformed zones are more than dynamically recrystallized zones. Pan et al. (2019) demonstrated that LAGBs are capable of hindering the motion of dislocations, leading to a certain amount of strengthening. Besides, as we all know, nano-sized particles that appear due to dynamic precipitation in the extrusion process could be an obstacle of dislocation on the basis of the Orowan mechanism (Ma et al., 2014), and that strength was increased due to the presence of nano-scaled Mg_3Bi_2 precipitates.

The fracture surface of specimen after tensile test exhibits well-proportional dimples and tear ridges on the surface of the tensile fracture, validating the much higher ductility compared to those of recently reported extrusion Mg-based alloys such as Mg-1Sn-0.2Ca alloy (Zhao et al., 2016) or Mg-RE systems (Mg-3Nd-0.2Zn-0.4Zr alloy) (Zhang et al., 2012). Generally, the basal slip system basically dominates the deformation of Mg alloys at room temperature. On the one hand, the structure of relatively fine-DRXed grains accompanied with elongated grains is conducive to the dislocation slip and then leads to a higher strain coordination capability among grains during plastic deformation. On the other hand, the average Schmid factor of the

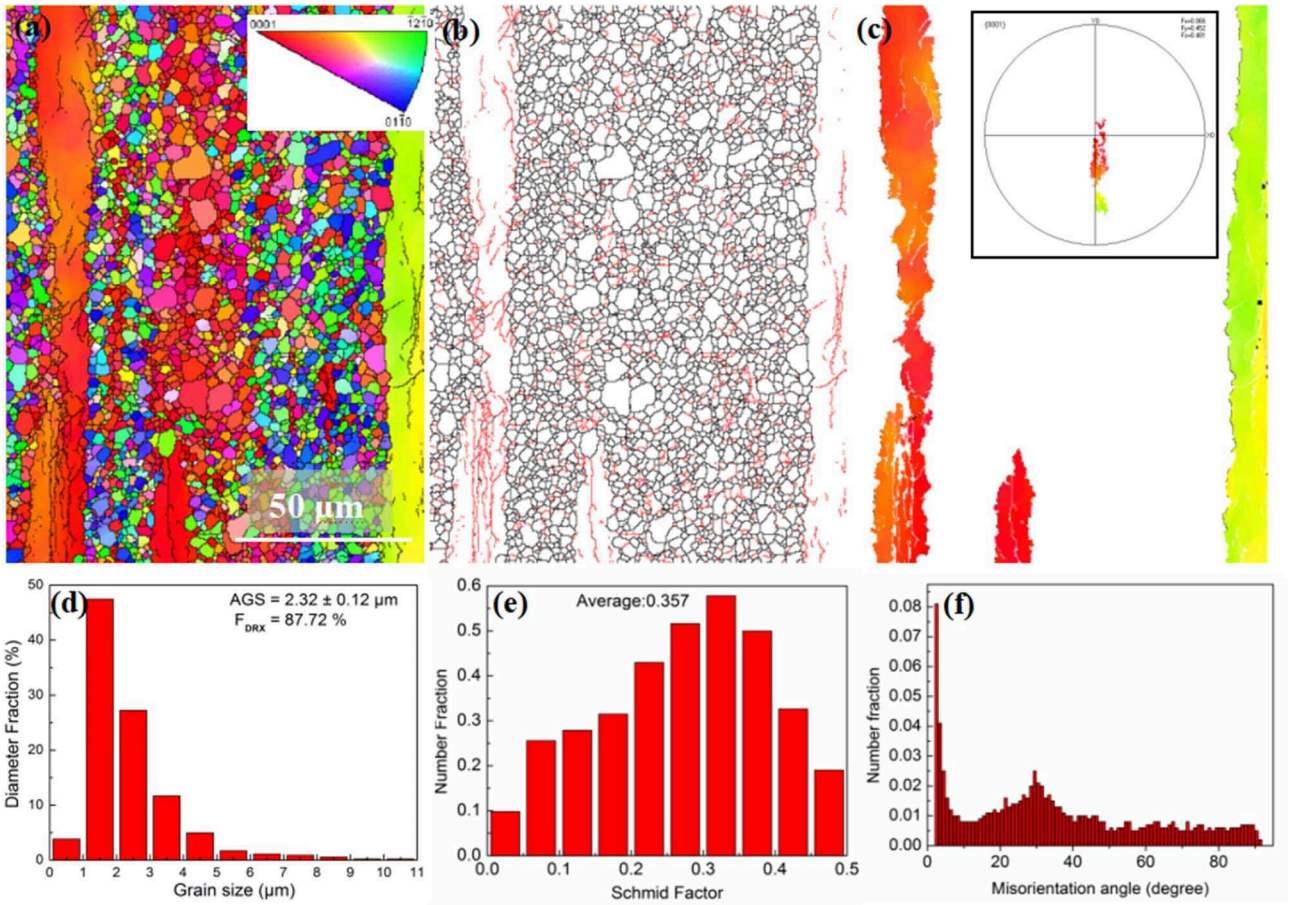

FIGURE 1 | EBSD observation results of the extruded alloy: **(a)** inverse pole figure (IPF) map (the inserted stereographic triangle corresponds to the crystallographic axes of the grains), **(b)** grain boundary map, **(c)** inverse pole figure in three regions containing only elongated grains with the corresponding (0001) pole figure inserted in it, **(d)** grain size distribution, **(e)** (0001) <1120> basal slip Schmid factor distribution histograms, and **(f)** misorientation angle distribution.

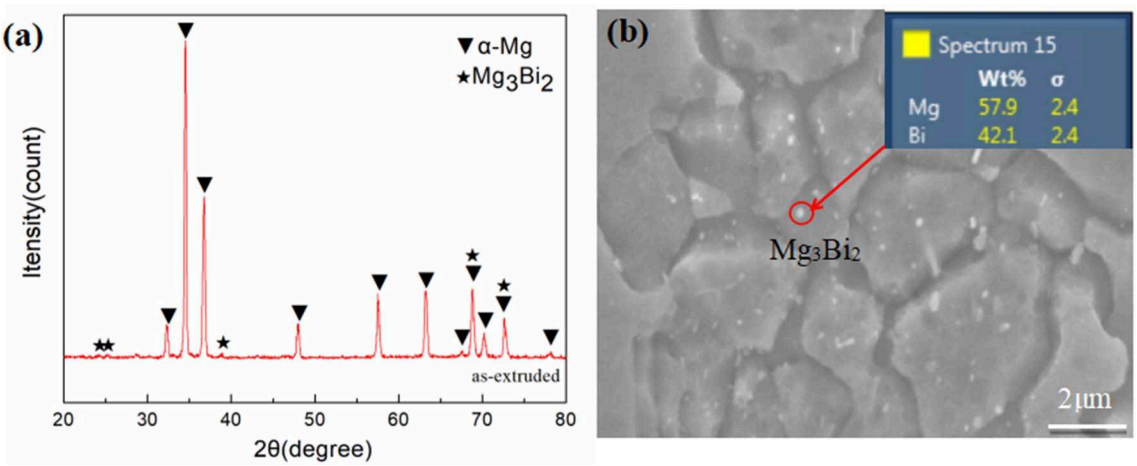

FIGURE 2 | X-ray diffraction patterns **(a)**, SEM high-magnification image with EDS results of studied alloy **(b)**.

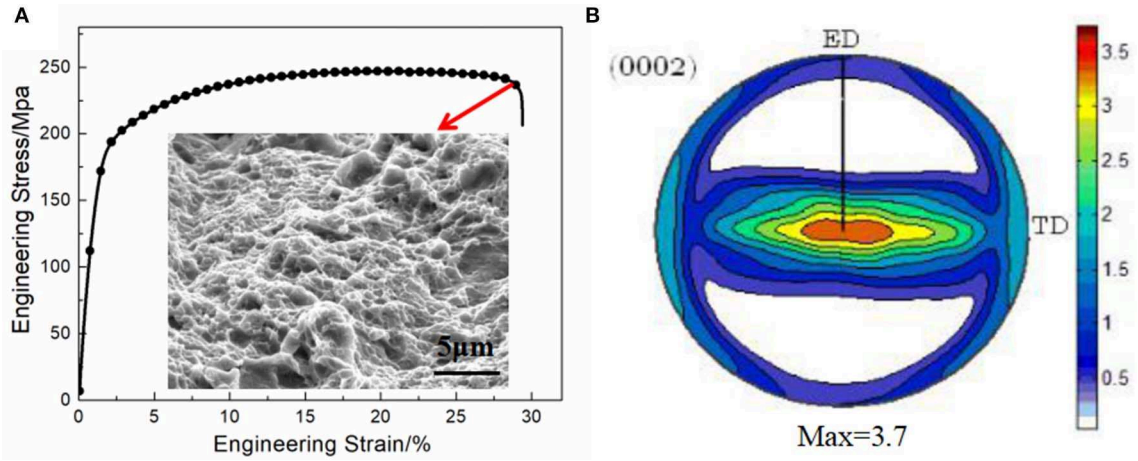

FIGURE 3 | The engineering stress–strain curves with fracture surface of the tensile sample **(A)** and the (0002) pole figure **(B)** of the extruded alloy.

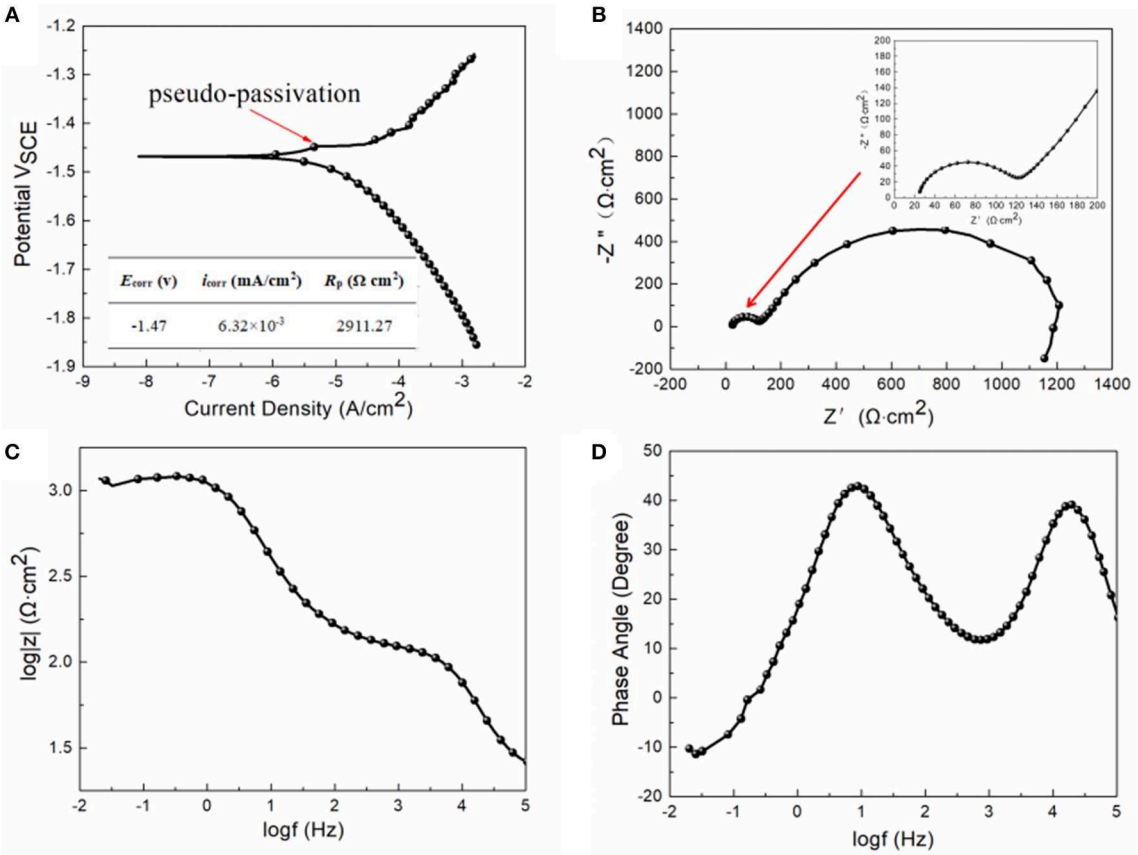

FIGURE 4 | The polarization curve with electrochemical parameters obtained from the potentiodynamic polarization test **(A)**, Nyquist plot with image of local area appended on the upper right corner **(B)**, Bode plot of impedance vs. frequency **(C)**, and Bode plot of phase angle vs. frequency **(D)** for the extruded alloy measured in the SBF solution at room temperature.

present extruded alloy being 0.357 is beneficial to the activation of basal slip and thus a higher ductility. Moreover, the larger value of the work-hardening exponent makes alloy less sensitive to strain localization, and the extruded alloy exhibits a work-hardening exponent of 0.23 ($\sigma = K\varepsilon^n$) using the Hollomon equation, which is partially related to a superior elongation.

Corrosion Behavior

Electrochemical Results

Figure 4A shows the PDP curve of as-extruded alloy attained via testing in SBF solution, accompanied by values of corrosion current density (i_{corr}), corrosion potential (E_{corr}), and polarization resistance (R_p). It is noticeable that there is a slight pseudo-passivation in the anodic branch of polarization curve for the alloy, as the protective film containing magnesium phosphate is formed, with appearance of breakdown potential at −1.448 V_{SCE}. The cathode branch is a result of hydrogen evolution reaction and the small density of the cathodic current implying hydrogen evolution at a low rate. Besides, based on the equation, the studied alloy is found to have a corrosion rate (P_i) of 0.14 mm/a, which is much lower than the standard value of 0.5 mm/a for the biodegradable implant Mg-based alloys (Erinc et al., 2009). This is possibly related to the fine-grained structure of the studied alloy (AGS of the DRXed grain is about 2.32 μm). The grain boundaries act as corrosion barriers, which is attributed to the more negative corrosion potential and forms products of corrosion and thus resulted in decreasing corrosion rate (Alvarez-Lopez et al., 2010). The fine-grained structure, namely, relatively abundant grain boundaries of the extruded alloy, may lead to a decrease in the corrosion rate. In addition, some formation of LAGBs (sub-grain) is verified using distribution of misorientation angles in **Figure 1e**, from which we found a high peak of 2–15°. Hu et al. (2017) reported that alloys with a higher proportion of LAGBs exhibit better corrosion resistance. Compared with the LAGBs, high-angle grain boundaries (HAGBs) are supposed to possess higher reactivity and are more susceptible to anodic dissolution. As a result, during the development of pitting corrosion, HAGBs serve as effective anodes and are preferentially attacked (Cao et al., 2019). Thus, corrosion resistance is enhanced in view of the higher fraction of LAGBs in the α-Mg matrix. Further work will shed light on the correlation between corrosion properties and low-angle grain boundaries.

As exhibited, the Nyquist plot (**Figure 4B**) contains a little capacitive loop in a region of high frequency (local-area inset in the upper right corner), and then a secondary great capacitive loop in regions of medium and low frequencies.

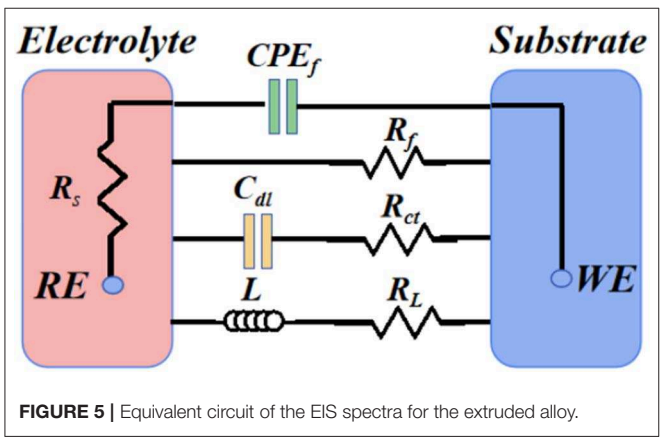

FIGURE 5 | Equivalent circuit of the EIS spectra for the extruded alloy.

TABLE 2 | Electrochemical parameters of the extruded alloy, obtained from the simulation of EIS date by using equivalent circuits.

Specimen	R_s (Ω cm^2)	CPE_f (F/cm^2)		R_f (Ω cm^2)	CPE_{dl} (F/cm^2)		R_{ct} (Ω cm^2)	L (H/cm^2)	R_L (Ω cm^2)
		CPE_f-I	n		CPE_{dl}-I	n			
Extruded	24.8	2.07×10^{-7}	0.9953	29.12	7.27×10^{-5}	0.8121	1257	513	617

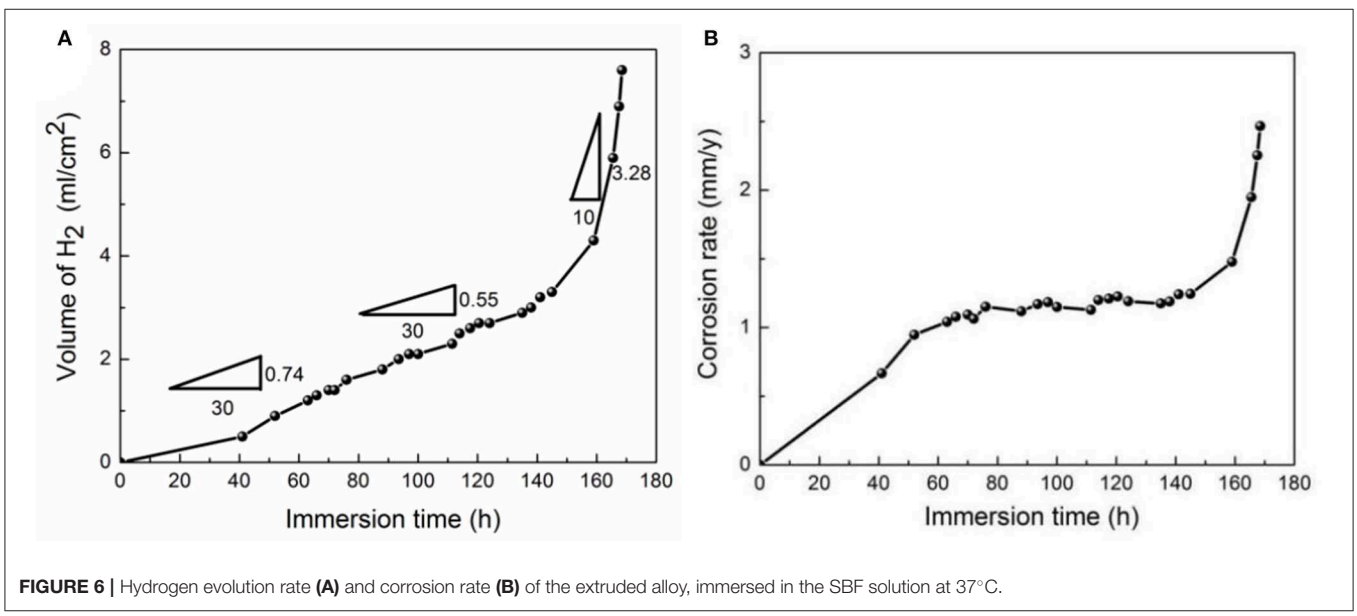

FIGURE 6 | Hydrogen evolution rate **(A)** and corrosion rate **(B)** of the extruded alloy, immersed in the SBF solution at 37°C.

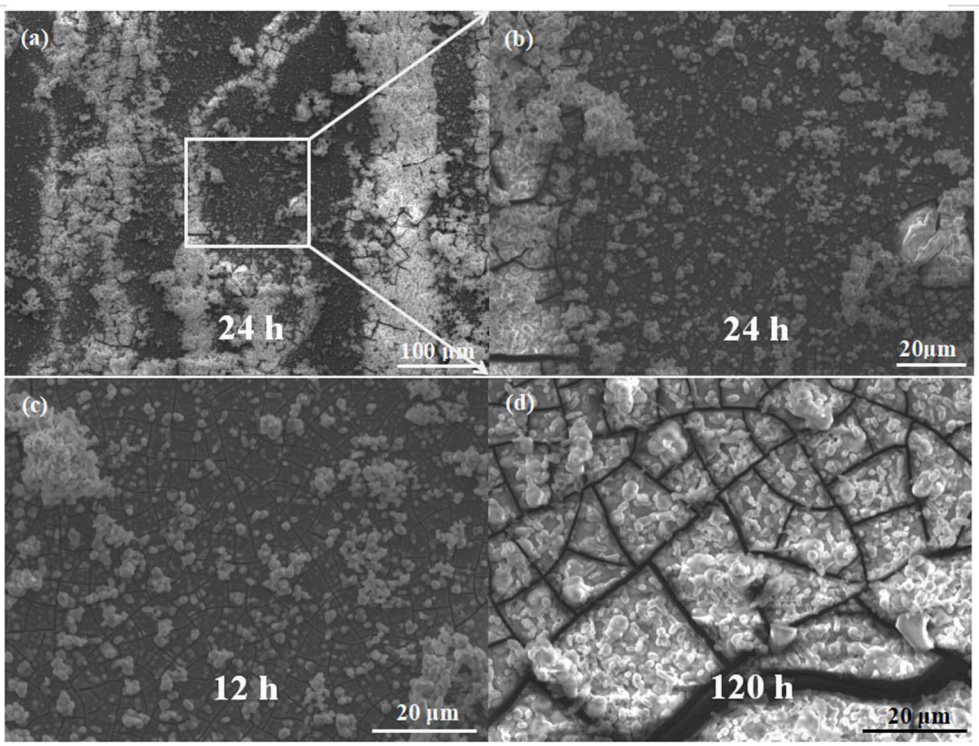

FIGURE 7 | Surface SEM images of corrosion products of the extruded alloy **(a)** and the high-magnification SEM images from a local area corresponding to the immersion time of 24 h **(b)**, 12 h **(c)**, and 120 h **(d)**.

Generally, the capacitive loop in regions of high frequencies is a result of relaxation of electrochemical impedance reaction that corresponds to specimen degradation. The capacitive loop in the region of low frequencies is associated with the existence of a surface film, which influences corrosion (Jayaraj et al., 2016). The plots in the region of lower frequencies apart from the region of capacitive loop with low frequencies contribute to pitting corrosion during corrosion. The Bode plot for impedance and frequency is shown in **Figure 4C**. In general, a larger impedance modulus $|Z|$ reveals better corrosion resistance, which is associated with the diameter of a greater capacitance arc. The Bode plot of phase angle vs. frequency is shown in **Figure 4D**, from which one can observe two apparent wave peaks at high frequency as well as medium and low frequencies of extruded alloy. The high-frequency spectra are associated with defects on the surface, and the low-to-medium frequency region is related to the process happening in corrosion products on an interface between the metal and the corrosion products.

To further analyze spectra of the studied alloy, **Figure 5** displays corresponding equivalent circuits and **Table 2** provides fitting data. The R_s and R_f in equivalent circuits refer to solution resistance and resistance of the layer of corrosion products, respectively, CPE_f is associated with surface heterogeneity. Generally speaking, the electrical double-layer capacitance (C_{dl}) is related to the metal surface–corrosive media interface. However, the constant phase element (CPE_{dl}) is used to replace the capacitance (C_{dl}) in consideration of the non-homogeneity of the surface. The charge transfer resistance (R_{ct}) is employed to describe the corrosion of surfaces. Furthermore, the inductance (L) and inductive resistance (R_L) are related to pitting corrosion and breakdown of corrosion layers (Feng et al., 2017).

Immersion Tests

Hydrogen evolution rates of the extruded alloy are demonstrated in **Figure 6A**, which indicates that the rate increases with increasing immersion time. The change of hydrogen evolution rate involves three phases: In the initial 60 h of immersion, the curves increase at a low rate of 0.025 of positive shift. In the immersion from 60 to 150 h, the hydrogen evolution rate is at a lower positive shift rate of 0.018. Prolonged immersion time leads to a relative higher shift rate of 0.328 from 150 to 168 h. Corrosion rate of extruded alloys is found to be relatively stable from 60 to 150 h compared to other immersion time periods (**Figure 6B**).

To figure out the relation of hydrogen evolution rate with corrosive behavior, **Figure 7** illustrates surface morphologies of extruded alloy immersed in SBF solution for different durations. The formation of products of corrosion after 24 h of immersion can be observed preferentially along the direction of extrusion in **Figure 7a**, while the large flocculent and tabular corrosion products are mostly formed near the unDRXed region and some cracks are obviously presented in the α-Mg and corrosion products. **Figure 7b** shows that even though several microcracks can be seen in the DRXed region, the corrosion product

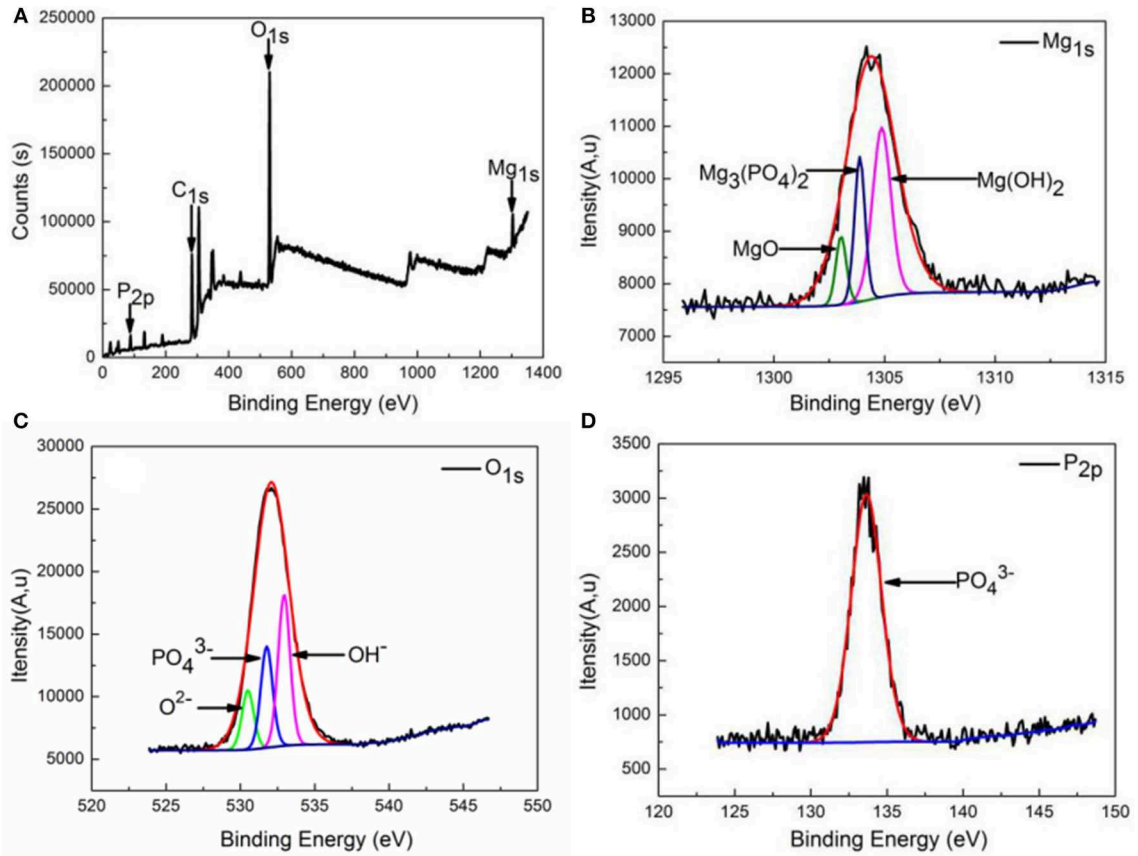

FIGURE 8 | XPS analysis of the formed corrosion product film on the extruded alloy surface: **(A)** wide spectrum, **(B)** high-resolution Mg_{1s} spectrum, **(C)** high-resolution O_{1s} spectrum, and **(D)** high-resolution P_{2p} spectrum.

formed in the DRXed region is relatively few compared to that adjacent to the unDRXed region. The SEM observations of extruded alloys after 12 h of immersion in SBF solution are illustrated in **Figure 7c**, which shows that the specimen surface is characterized by some uneven cracks and the white corrosion product particles are distributed at boundaries and in the interior of grains. Moreover, the prolonged immersion time resulted in the increased amount and dimension of the clotty corrosion product particles, the surface of the specimen is mainly composed of corrosion products gradually, and then the local massive products are linked together and a layer of thin union corrosion product film is formed, which gradually thickens with the increase in immersion time. This film can prevent the solution permeating into the α-Mg matrix. Finally, the corrosion product film is broken with increasing immersion time, and lots of network cracks can be observed in the corrosion products after 120 h of immersion of specimens in SBF solution (**Figure 7d**).

XPS spectra for surfaces formed on extruded alloy by immersing the alloy in SBF solution for 1 h at 37°C are shown in **Figure 8** to further confirm the composition of the products. The XPS spectra (**Figure 8A**) reveal the existence of Mg, O, C, and P in corrosion products formed on surfaces of as-extruded alloy. As indicated, the Mg_{1s} spectra are found to have three peaks. Binding energies at 1303.04, 1303.88, and 1304.87 eV are attributable to MgO, $Mg_3(PO_4)_2$, and $Mg(OH)_2$, respectively. The result means Mg forming MgO, $Mg_3(PO_4)_2$, and $Mg(OH)_2$ on extruded alloy surfaces. From **Figure 8C**, it is obvious that there are three peaks on O_{1s} spectrum, oxygen in oxides (530.48 eV) is indicative of MgO, oxygen (531.78 eV) corresponds to $Mg_3(PO_4)_2$, and the oxygen in hydroxyl groups (532.98 eV) corresponds to $Mg(OH)_2$. **Figure 8D** shows the binding energy of P_{2p} at about 133.65 eV, which is associated with formation of $Mg_3(PO_4)_2$.

Based on the analysis of the corrosion product on surfaces of immersed specimen and curves of hydrogen evolution of extruded alloy, the early stage witnesses a rapid hydrogen evolution in **Figure 6A**; the dissolution of the α-Mg matrix leads to the formation of corrosion products (**Figure 7c**), which comprise $Mg_3(PO_4)_2$ and $Mg(OH)_2$ (**Figure 8**). According to Zeng et al. (2014), the lower enthalpy values of oxide formation indicate greater chemical, and it is generally accepted that $Mg_3(PO_4)_2$ and $Mg(OH)_2$ are relatively more stable than MgO. In addition, Pilling–Bedworth ratio (PBR), which is representative of the stress state of the oxide film, indicates that insufficient oxide is present to cover and protect the metal when PBR is <1. Thus, $Mg_3(PO_4)_2$ and $Mg(OH)_2$ with

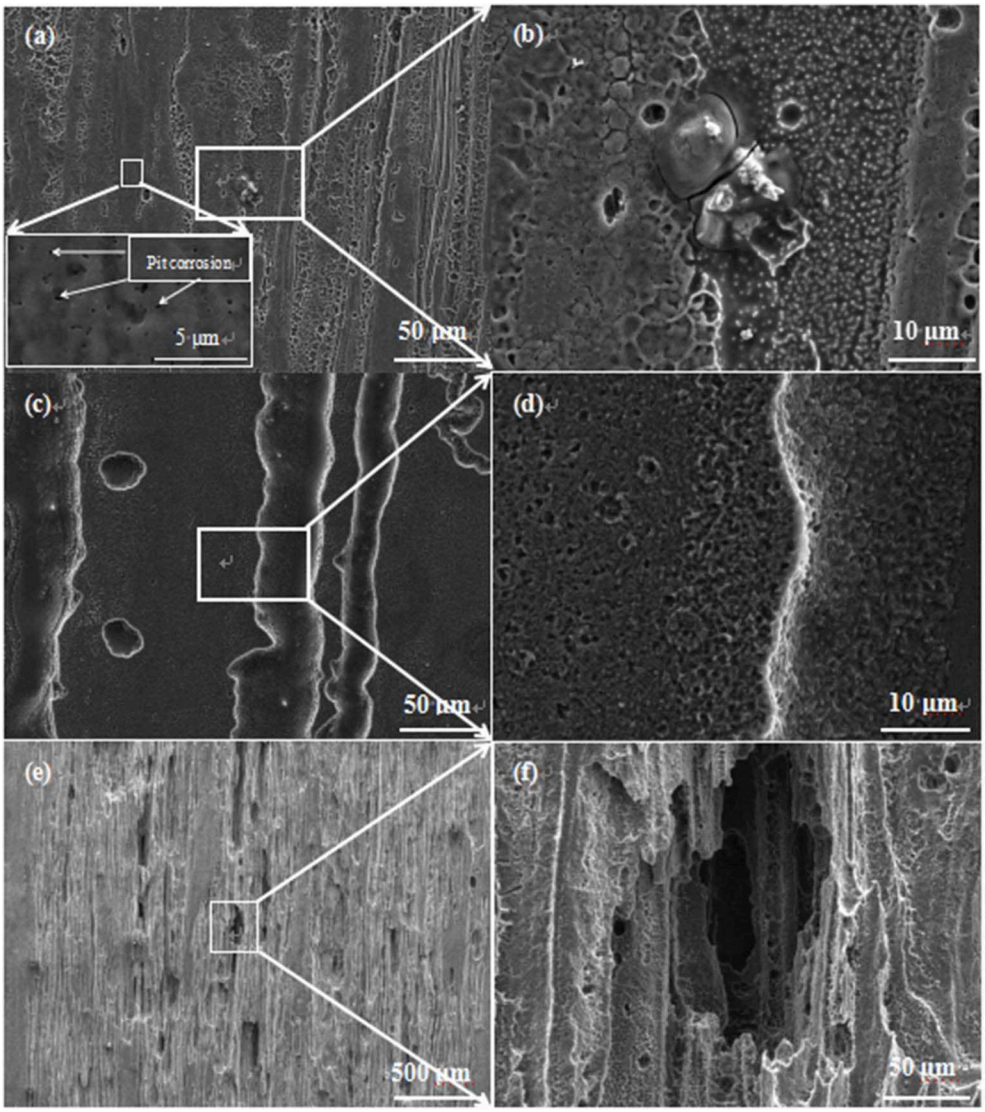

FIGURE 9 | Surface SEM micrographs of the extruded alloy, after being immersed in the SBF solution at 37°C: the extruded alloy **(a,b)** 12 min, **(c,d)** 12 h, and **(e,f)** 120 h.

PBR values of 2.29 and 1.80, respectively, indicate a dense and protective layer of the corrosion product on the studied alloy. After immersion for ∼60 h, the hydrogen evolution rate is reduced a little due to the formation of a union film of corrosion products on specimen surfaces. Growth and healing of the film represent main effective processes, which can further prevent the SBF solution penetrating into the α-Mg matrix when the film layer becomes thickened and compacted. However, the film will shrink when $Mg(OH)_2$ connects with H_2O inside the film, leading to dehydration, and this shrinkage stress will give rise to the crack formation in the corrosion product film as shown in **Figure 7d**, and the SBF solution will penetrate these cracks and then the new corrosion products will form by means of reaction with the α-Mg matrix. With immersion time exceeding 150 h, the dissolution rate of film surpasses its healing rate, and the intensified corrosion attack on the surface will result in the hydrogen evolution rate increasing rapidly (**Figure 6A**).

Figure 9 shows SEM images for surfaces of extruded alloy immersed in SBF solution for different durations (12 min, 12 h, and 120 h), which reveals the potential microstructure to be analyzed after corrosion. The corrosion in **Figure 9a** occurs in the vicinity of the unDRXed region and the slight corrosion striation along the ED. Furthermore, there is several corrosion pit in the DRXed region, which is mainly attributed to the nano-scaled precipitates acting as the microgalvanic cathode with respect to the α-Mg matrix; thus, pit corrosion is formed by microgalvanic corrosion. It is worth reminding that the degree of corrosion in the unDRXed region is different, which could be observed from the high-magnification image of the local

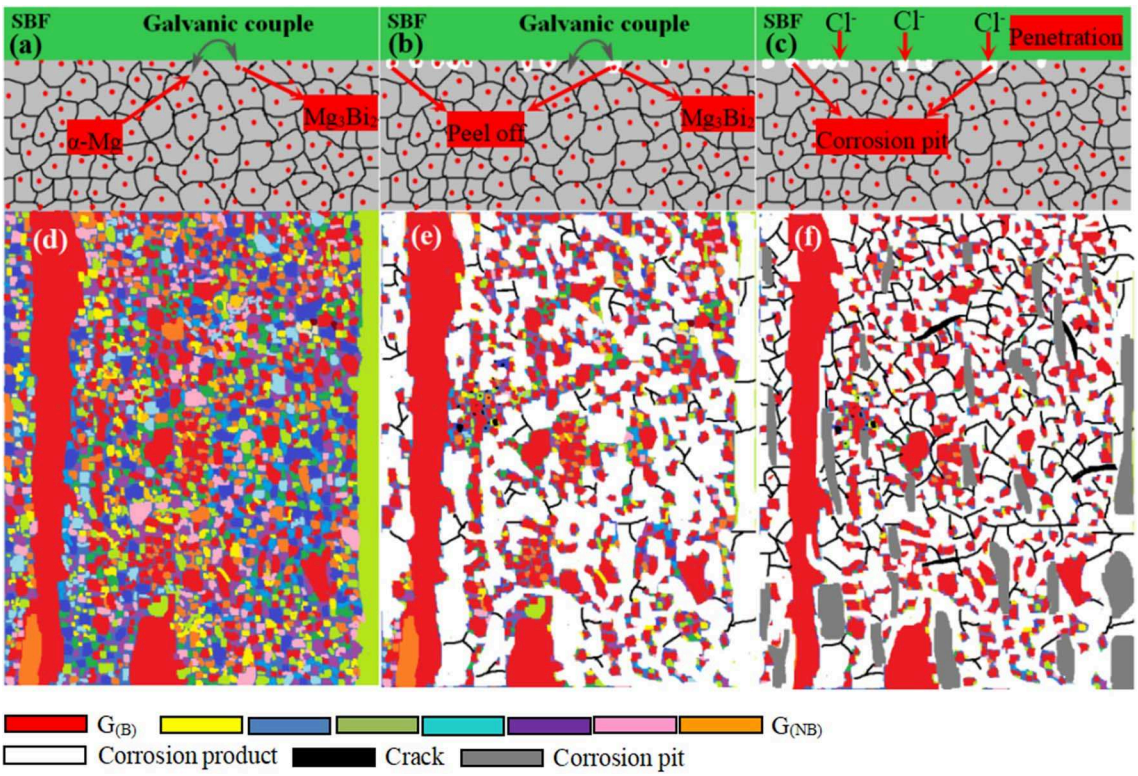

FIGURE 10 | The schematic illustration of the extruded alloy during the corrosion process: **(a,d)** the initial immersion; **(b,e)** the middle immersion and **(c,f)** the final immersion of studied alloy. α-Mg grains representing basal (B) crystal orientations where regions in red were referred as $G_{(B)}$ with non-basal (NB) crystal planes where regions in other color were referred as $G_{(NB)}$.

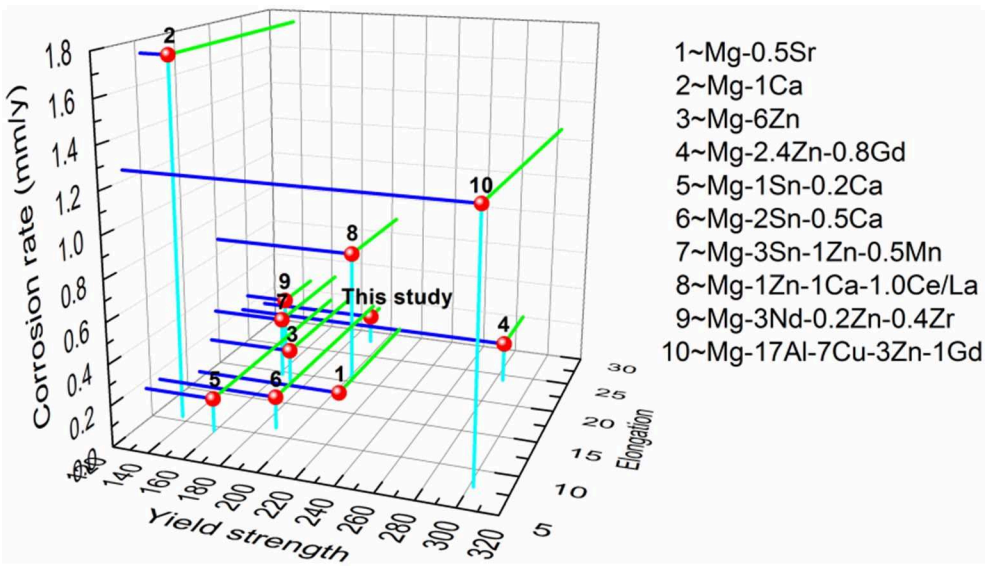

FIGURE 11 | The performance matrix used to compare the mechanical properties and corrosion behavior of extruded alloy with previously reported Mg-based alloy systems.

area (**Figure 9b**). The results indicate that $G_{(NB)}$ suffers from a severe attack compared to $G_{(B)}$, as shown in **Figure 1c**, where regions in red indicated that the grains present better corrosion resistance while regions in cyan exhibit rapid corrosion rate. Besides, formation of small corrosion pits in the DRXed region is attributed to the dissolution in individual $G_{(NB)}$. It is generally

supposed that the basal crystal orientation (0001) possessed the best corrosion resistance among all the crystal orientation, which was attributed to a cooperative effect of the surface energy, atomic packing density, and the stability of oxidation film (Hagihara et al., 2016). Jia et al. (2018) also reported that the longitudinal direction with more (0002) oriented planes had a lower corrosion current density of 35.9 $\mu A/cm^2$ compared with the transverse direction. Thus, in comparison with $G_{(NB)}$, the dissolution rate of Mg in $G_{(B)}$ is substantially lower. Moreover, as shown in **Figure 9c**, the corrosion region becomes obviously deeper with the prolonged corrosion time and a number of finer pits that formed due to corrosion are seen in areas of inconspicuous corrosion (**Figure 9d**), which could verify Mg grains being dissolved preferentially following prismatic crystal faces in $G_{(NB)}$. Finally, with an increase of the reaction time, a more fringe shape appears on the surface of the specimen in **Figure 9e**. The highly magnified image (**Figure 9f**) clearly shows evidence for cavity structures in the local region.

Corrosion Mechanism

It can be seen from **Figures 10a,d** that clotty products of corrosion form near nano-scaled Mg_3Bi_2 precipitates and the $G_{(NB)}$, when the corrosion products are sufficient enough to link together, and the layer of product film is formed subsequently on the surface of the α-Mg matrix. This union protective film can prevent caustic ion from the SBF solution permeating into the α-Mg matrix. The chemical reactions that usually occur during this process are as follows:

$$Mg \rightarrow Mg^{2+} + 2e^{-} \text{(anodic reaction)} \quad (4)$$

$$2H_2O + 2e^{-} \rightarrow H_2\uparrow + 2OH^{-} \text{(cathodic reaction)} \quad (5)$$

$$Mg^{2+} + 2OH^{-} \rightarrow Mg(OH)_2 \text{(corrosion product formation)} \quad (6)$$

$$3Mg^{2+} + 2PO_4^{3-} \rightarrow Mg_3(PO_4)_2 \text{(corrosion product formation)} \quad (7)$$

With prolonged immersion time, the degradation rate exceeds the healing and growth ability of the protective film, the crack occurs in the corrosion product film, and the film is damaged (**Figures 10b,e**, respectively). In general, microgalvanic corrosion is easily activated due to the presence of the nano-scaled Mg_3Bi_2 precipitate, which acts as a microgalvanic cathode with regard to the α-Mg matrix. As the corrosion process proceeded, the Mg_3Bi_2 phase particle would be exfoliated off from surfaces of the α-Mg matrix, leading to formation of cracks nearby. Furthermore, microgalvanic corrosion is also formed between $G_{(NB)}$ and $G_{(B)}$, with $G_{(NB)}$ being of micro-cathode, and the $G_{(NB)}$ grains peel off and lead to the formation of a corrosion pit. Finally, relatively serious localized corrosion occurs in the extruded alloy (**Figures 10c,f**), leaving some corrosion pit and network cracks on the surface.

Properties Comparison

The performance comparison between the present extruded alloy and other extruded alloys (Laser et al., 2008; Li et al., 2008; Zhang et al., 2010; Ma et al., 2014; Geng et al., 2016; Hou et al., 2016; Tong et al., 2016; Miao et al., 2017; Zhao et al., 2017) is shown in **Figure 11**. It should be noted that the present extruded low-alloyed alloy has a better YS (YS = 201 MPa) than that of the recently reported extruded Mg alloys such as Mg-6Zn (YS = 170 MPa) (Zhao et al., 2017), Mg-2Sn-0.5Ca (YS = 188 MPa) (Laser et al., 2008), Mg-3Sn-1Zn-0.5Mn (YS = 162 MPa) (Hou et al., 2016), and Mg-3Nd-0.2Zn-0.4Zr (YS = 145 MPa) (Ma et al., 2014). In addition, the extruded alloy with an average DRXed grain size of 2.32 μm has a favorable corrosion resistance compared to the other fine-grained extruded alloy. The corrosion rates of Mg-2.4Zn-0.8Gd alloy (Miao et al., 2017) (average size of ∼3.00 μm of DRXed grains) and Mg-1Zn-1Ca-1Ce/La alloy (Tong et al., 2016) (average size of ∼4.00 μm of DRXed grains) are 0.2 and 0.68 mm/a, respectively, which are higher than that of the studied alloy system (P_i = 0.14 mm/a). Thus, it is of great potential to develop the low-alloyed Mg-Bi-Al-Zn alloy as materials for producing biomedical implants.

CONCLUSIONS

(1) The low-alloyed Mg-Bi-Al-Zn system has a distinguished combination of ductility and strength mainly because of bimodal grain structure and dispersed nano-scale Mg_3Bi_2 particles.

(2) The corrosion behavior of the low-alloyed Mg-Bi-Al-Zn system is greatly dependent on the grain orientation and corrosion product film. The propagation of corrosion in non-basal Mg grains is more apparent than basal ones. The corrosion product film healing and growth can further prevent the SBF solution penetrating into the α-Mg matrix, while the shrinkage stress will give rise to the crack formation in the corrosion product film.

(3) The present low-alloyed Mg-Bi-Al-Zn system is expected to be a potential candidate as an implant material with preferable combination of tensile properties and corrosion resistance.

DATA AVAILABILITY STATEMENT

The datasets generated for this study are available on request to the corresponding author.

AUTHOR CONTRIBUTIONS

WC provided detailed guidance to this paper. YL wrote the manuscript. SM completed the experimental part of the paper. LW modified the language of this paper. HW provided technical support for this paper. XN provided financial support for this paper.

FUNDING

This study was jointly supported by the National Natural Science Foundation of China (Grant Nos. 51704209 and 51701060), the Natural Science Foundation of Shanxi (201801D121088), a Research Project Supported by Shanxi Scholarship Council of China (Grant No. 2014-023), and the Shanxi Province Science Foundation for Youths (Grant No. 2016021063).

REFERENCES

Alvarez-Lopez, M., Pereda, M. D., Valle, J. A., Fernandez-Lorenzo, M., Garcia-Alonso, M. C., Ruano, O. A., et al. (2010). Corrosion behaviour of AZ31 magnesium alloy with different grain sizes in simulated biological fluids. *Acta Biomater.* 6, 1763–1771. doi: 10.1016/j.actbio.2009.04.041

Argade, G. R., Panigrahi, S. K., and Mishra, R. S. (2012). Effects of grain size on the corrosion resistance of wrought magnesium alloys containing neodymium. *Corros. Sci.* 58, 145–151. doi: 10.1016/j.corsci.2012.01.021

Bakhsheshi-Rad, H. R., Hamzah, E., Kasiri-Asgarani, M., Safaa Saud, N., Yaghoubidoust, F., and Akbari, E. (2016). Structure, corrosion behavior, and antibacterial properties of nanosilica/graphene oxide coating on biodegradable magnesium alloy for biomedical applications. *Vacuum* 131, 106–110. doi: 10.1016/j.vacuum.2016.05.021

Cao, C., Chen, D. B., Ren, J. K., Shen, J. G., Meng, L., and Liu, J. B. (2019). Improved strength and enhanced pitting corrosion resistance of Al-Mn alloy with Zr addition. *Mater. Lett.* 255:126535. doi: 10.1016/j.matlet.2019.126535

Cheng, W. L., Tian, L., Wang, H. X., Bian, L. P., and Yu, H. (2017). Improved tensile properties of an equal channel angular pressed (ECAPed) Mg-8Sn-6Zn-2Al alloy by prior aging treatment. *Mater. Sci. Eng. A* 687, 148–154. doi: 10.1016/j.msea.2017.01.054

Erinc, M., Sillekens, W. H., Mantens, G., and Werkhoven, R. (2009). Applicability of existing magnesium alloys as biomedical implant materials. *Magnesium Technol.* 14, 209–202.

Esmaily, M., Svensson, J. E., Fajardo, S., Birbilis, N., Frankel, G. S., Virtanen, S., et al. (2017). Fundamentals and advances in magnesium alloy corrosion. *Prog. Mater. Sci.* 89, 92–193. doi: 10.1016/j.pmatsci.2017.04.011

Feng, H., Liu, S. H., Du, Y., Lei, T., Zeng, R. C., and Yuan, T. C. (2017). Effect of the second phases on the corrosion behavior of the Mg-Al-Zn alloys. *J. Alloys Compd.* 695, 2330–2338. doi: 10.1016/j.jallcom.2016.11.100

Geng, Z. W., Xiao, D. H., and Chen, L. (2016). Microstructure, mechanical properties, and corrosion behavior of degradable Mg-Al-Cu-Zn-Gd alloys. *J. Alloys Compd.* 686, 145–152. doi: 10.1016/j.jallcom.2016.05.288

Goli, E., and Aghajani, H. (2018). A study on corrosion resistance of Al magnetron sputtering coatedAZ31 magnesium alloy. *Vacuum* 152, 231–238. doi: 10.1016/j.vacuum.2018.03.032

Hagihara, K., Okubo, M., Yamasaki, M., and Nakano, T. (2016). Crystal-orientation-dependent corrosion behaviour of single crystals of a pure Mg and Mg-Al and Mg-Cu solid solutions. *Corros. Sci.* 109, 68–85. doi: 10.1016/j.corsci.2016.03.019

He, C., Liu, C. Q., Chen, H. W., and Nie, J. F. (2019). Enhanced age-hardening response in Mg-Zn-Co alloys with Bi additions. *J. Alloys Compd.* 815:152419. doi: 10.1016/j.jallcom.2019.152419

Hou, L. D., Li, Z., Zhao, H., Pan, Y., Pavlinich, S., Liu, X. W., et al. (2016). Microstructure, mechanical properties, corrosion behavior and biocompatibility of extruded biodegradable Mg-3Sn-1Zn-0.5Mn alloy. *J. Mater. Sci. Technol.* 32, 874–882. doi: 10.1016/j.jmst.2016.07.004

Hu, Y. B., Zhang, C., Meng, W. Q., Pan, F. S., and Zhou, J. P. (2017). Microstructure, mechanical and corrosion properties of Mg-4Al-2Sn-χY-0.4Mn alloys. *J. Alloys Compd.* 27, 491–500. doi: 10.1016/j.jallcom.2017.08.171

Jayaraj, J., Raj, S. A., Srinivasan, A., Ananthakumar, S. U., Pilai, T. S., Dhaipule, N. G. K., et al. (2016). Composite magnesium phosphate coatings for improved corrosion resistance of magnesium AZ31 alloy. *Corros. Sci.* 113, 104–115. doi: 10.1016/j.corsci.2016.10.010

Jia, H., Feng, X., and Yang, Y. (2018). Effect of crystal orientation on corrosion behavior of directionally solidified Mg-4 wt.% Zn alloy. *J. Mater. Sci. Technol.* 34, 1229–1235. doi: 10.1016/j.jmst.2017.06.009

Jina, Y., Blawert, C., Feyerabend, F., Bohlen, J., Campos, M., Gavras, S., et al. (2019). Time-sequential corrosion behaviour observation of micro-alloyed Mg-0.5Zn-0.2Ca alloy via a quasi-in situ approach. *Corros. Sci.* 158:108096. doi: 10.1016/j.corsci.2019.108096

Laser, T., Hartig, C., Nurnberg, M. R., Letzig, D., and Bormann, R. (2008). The influence of calcium and cerium mischmetal on the microstructural evolution of Mg−3Al−1Zn during extrusion and resulting mechanical properties. *Acta Mater.* 56, 2791–2798. doi: 10.1016/j.actamat.2008.02.010

Li, Z. J., Gu, X. N., Lou, S. Q., and Zheng, Y. F. (2008). The development of binary Mg-Ca alloys for use as biodegradable materials within bone. *Biomaterials* 29, 1329–1344. doi: 10.1016/j.biomaterials.2007.12.021

Liu, Q., Ma, Q. X., Chen, G. Q., Cao, X., Zhang, S., Pan, J. L., et al. (2018). Enhanced corrosion resistance of AZ91 magnesium alloy through refinement and homogenization of surface microstructure by friction stir processing. *Corros. Sci.* 138, 284–296. doi: 10.1016/j.corsci.2018.04.028

Luo, Y., Deng, Y., Guan, L., Ye, L., and Guo, X. (2020). The microstructure and corrosion resistance of as-extruded Mg-6Gd-2Y-(01.5) Nd-0.2Zr alloys. *Mater. Des.* 186:108289. doi: 10.1016/j.matdes.2019.108289

Lv, S. H., Lü, X. L., Meng, F. Z., Yang, Q., Qiu, X., Qin, P. F., et al. (2020). Microstructures and mechanical properties in a Gd-modified high-pressure die casting Mg-4Al-3La-0.3Mn alloy. *Mater. Sci. Eng. A* 773:138725. doi: 10.1016/j.msea.2019.138725

Ma, K., Wen, H., Hu, T., Topping, T. D., Isheim, D., Seidman, D. N., et al. (2014). Mechanical behavior and strengthening mechanisms in ultrafine grain precipitation-strengthened aluminum alloy. *Acta Mater.* 62, 141–155. doi: 10.1016/j.actamat.2013.09.042

Majhi, J., and Mondal, A. K. (2019). Microstructure and impression creep characteristics of squeeze-cast AZ91 magnesium alloy containing Ca and/or Bi. *Mater. Sci. Eng. A* 744, 691–703. doi: 10.1016/j.msea.2018.12.067

Meng, S. J., Yu, H., Fan, S. D., Kim, Y. M., Park, S. H., Zhao, W. M., et al. (2020). A high-ductility extruded Mg-Bi-Ca alloy. *Mater. Lett.* 261:127066. doi: 10.1016/j.matlet.2019.127066

Miao, H. W., Huang, H., Shi, Y. J., Zhang, H., Pei, J., and Yuan, G. Y. (2017). Effects of solution treatment before extrusion on the microstructure, mechanical properties and corrosion of Mg-Zn-Gd alloy *in vitro*. *Corros. Sci.* 122, 90–99. doi: 10.1016/j.corsci.2017.01.001

Pan, H. C., Kang, R., Li, J. R., Zeng, Z. R., Xie, H. B., Huang, Q. Y., et al. (2019). Mechanistic investigation of a low-alloy Mg-Ca-based extrusion alloy with high strength–ductility synergy. *Acta Mater.* 186, 278–290. doi: 10.1016/j.actamat.2020.01.017

Shi, Z., Liu, M., and Atrens, A. (2010). Measurement of the corrosion rate of magnesium alloys using Tafel extrapolation. *Corros. Sci.* 52, 579–588. doi: 10.1016/j.corsci.2009.10.016

Shi, Z. M., and Atrens, A. (2011). An innovative specimen configuration for the study of Mg corrosion. *Corros. Sci.* 53, 226–246. doi: 10.1016/j.corsci.2010.09.016

Tok, H. Y., Hamzah, E., and Bakhsheshi-Rad, H. R. (2015). The role of bismuth on the microstructure and corrosion behavior of ternary Mg-1.2Ca-xBi alloys for biomedical applications. *J. Alloys Compd.* 640, 335–346. doi: 10.1016/j.jallcom.2015.03.217

Tong, L. B., Zhang, Q. X., Jiang, Z. H., Zhang, J. B., Meng, J., Cheng, L. R., et al. (2016). Microstructures, mechanical properties and corrosion resistances of extruded Mg-Zn-Ca-*x*Ce/La alloys. *J. Mech. Behav. Biomed. Mater.* 62, 57–70. doi: 10.1016/j.jmbbm.2016.04.038

Wang, H., Yu, Z., Zhang, L., Liu, C., Zha, M., Wang, C., et al. (2015). Achieving high strength and high ductility in magnesium alloy using hard-plate rolling (HPR) process. *Sci. Rep.* 5:17100. doi: 10.1038/srep17100

Wang, M., Xiao, D. H., and Liu, W. S. (2017). Effect of Si addition on microstructure and properties of magnesium alloys with high Al and Zn contents. *Vacuum* 141, 144–151. doi: 10.1016/j.vacuum.2017.04.005

Yamasaki, M., Hashimoto, K., Hagihara, K., and Kawamura, Y. (2011). Effect of multimodal mi- crostructure evolution on mechanical properties of Mg-Zn-Y extruded alloy. *Acta Mater.* 59, 3646–3658. doi: 10.1016/j.actamat.2011.02.038

Zeng, R. C., Qi, W. C., Cui, H. Z., Zhang, F., Li, S. Q., and Han, E. H. (2015). *In vitro* corrosion of extruded Mg-Ca alloys—the influence of Ca concentration. *Corros. Sci.* 96, 23–31. doi: 10.1016/j.corsci.2015.03.018

Zeng, R. C., Sun, L., Zheng, Y. F., Cui, H. Z., and Han, E. H. (2014). Corrosion and characterisation of dual phase Mg–Li–Ca alloy in Hank's solution: The influence of microstructural features. *Corros. Sci.* 79, 69–82. doi: 10.1016/j.corsci.2013.10.028

Zhang, S. X., Zhang, X. N., Zhao, C. L., Li, J. A., Song, Y., Xie, C. Y., et al. (2010). Research on an Mg-Zn alloy as a degradable biomaterial. *Acta Biomater.* 6, 626–640. doi: 10.1016/j.actbio.2009.06.028

Zhang, X. B., Yuan, G. Y., Mao, L., Niu, J. L., Fu, P. H., and Ding, W. J. (2012). Effects of extrusion and heat treatment on the mechanical properties and biocorrosion behaviors of a Mg-Nd-Zn-Zr alloy. *J. Mech. Behav. Biomed. Mater.* 7, 77–86. doi: 10.1016/j.jmbbm.2011.05.026

Zhao, C. Y., Pan, F. S., and Pan, H. C. (2016). Microstructure, mechanical and bio-corrosion properties of extruded Mg-Sn-Ca alloys. *Trans. Nonferrous Met. Soc. China* 26, 1574–1582. doi: 10.1016/S1003-6326(16)64232-2

Zhao, C. Y., Pan, F. S., Zhang, L., Pan, H. C., Song, K., and Tang, A. T. (2017). Microstructure, mechanical properties, bio-corrosion properties and cytotoxicity of extruded Mg-Sr alloys. *Mater. Sci. Eng. C* 70, 1081–1088. doi: 10.1016/j.msec.2016.04.012

Conflict of Interest: The authors declare that the research was conducted in the absence of any commercial or financial relationships that could be construed as a potential conflict of interest.